Pressure Induced Amorphization of Pb^{2+} and Pb^{4+} in Perovskite $PbFeO_3$

Qiumin Liu,* Hena Das,* Takumi Nishikubo, Yuki Sakai, Ko Mibu, Tomoko Onoue, Takateru Kawakami, Tetsu Watanuki, Akihiko Machida, Xubin Ye, Jianhong Dai, Zhao Pan, Lei Hu, Satoshi Nakano, Masayuki Fukuda, Shiori Kihara, Koomok Lee, Takehiro Koike, Youwen Long, and Masaki Azuma*

Read Online

ACCESS | Metrics & More | Article Recommendations | Supporting Information

ABSTRACT: Perovskite-type oxides have been the subject of intense research due to their various fascinating physical properties stemming from their charge degree of freedom. $PbFeO_3$ has an unusual $Pb^{2+}_{0.5}Pb^{4+}_{0.5}Fe^{3+}O_3$ charge distribution with a long-ranged ordering of Pb^{2+} and Pb^{4+} and two inequivalent Fe^{3+} sites in a perovskite structure. Combined synchrotron X-ray diffraction and Mössbauer spectroscopy revealed a change to an orthorhombic $GdFeO_3$ structure with a unique Fe^{3+} site and randomly distributed Pb^{2+} and Pb^{4+} at 29.0 GPa, namely, pressure-induced amorphization of Pb^{2+} and Pb^{4+}. The absence of a charge transfer transition to the $Pb^{2+}Fe^{4+}O_3$ phase, which was expected from the comparison with $PbCrO_3$ and $PbCoO_3$, was verified using ab initio density functional theory calculations in the range of 0−70 GPa.
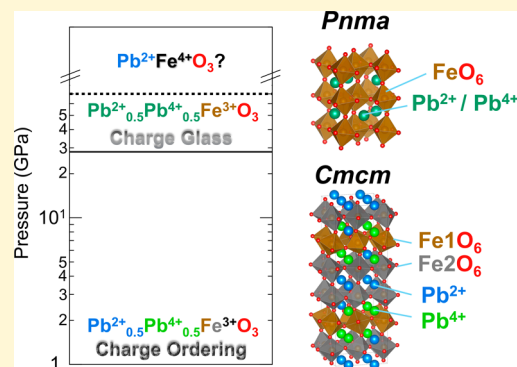
INTRODUCTION

The charge degrees of freedom exhibited by transition metal ions in the perovskite oxides have attracted great interest due to the various fascinating properties such as magneto-resistance,[1,2] metal−insulator transition,[3] and superconductivity.[4] Bi and Pb are not only main group elements but also have electronic configuration freedoms of $6s^2$ (Bi^{3+}, Pb^{2+}) and $6s^0$ (Bi^{5+}, Pb^{4+}). Because the $6s^1$ configurations (Bi^{4+}, Pb^{3+}) are prohibited, these are called valence-skipping ions or negative-U ions. We previously reported that the charge distribution of $BiMO_3$ and $PbMO_3$ (M: 3d transition metal ions) systematically changes depending on the position in the periodic table. As the atomic number of the 3d transition metal increases, the d-level becomes deeper and the valence decreases. Accordingly, Bi and Pb gradually change from $6s^2$ (Bi^{3+}, Pb^{2+}) to $6s^0$ (Bi^{5+}, Pb^{4+}).[5−19] The systematic change in the valence state distribution is due to the fact that the 6s level is close to the d levels of the transition metal and the 2p level of oxygen.

In Pb-based systems, tetragonal $PbTiO_3$ and $PbVO_3$ have $Pb^{2+}M^{4+}O_3$ charge distribution, while tetravalent lead is observed in $PbNiO_3$.[13,17,18] Other $PbMO_3$ exhibit charge-disproportionated Pb^{2+} and Pb^{4+} with average valences of Pb^{3+} or $Pb^{3.5+}$. In $PbCrO_3$, the coexistence of Pb^{2+} and Pb^{4+} without long-range ordering (charge glass) is observed. In this compound, due to the melting of the Pb charge disproportionation and simultaneous charge transfer between Pb^{4+} and Cr^{3+} at 2.5 GPa, a transition from insulating

$Pb^{2+}_{0.5}Pb^{4+}_{0.5}Cr^{3+}O_3$ to metallic $Pb^{2+}Cr^{4+}O_3$ accompanied by a large volume collapse occurs.[14] Further, complex charge distribution of $Pb^{2+}_{0.25}Pb^{4+}_{0.75}Co^{2+}_{0.5}Co^{3+}_{0.5}O_3$ with Pb^{2+}/Pb^{4+} and Co^{2+}/Co^{3+} orderings is present in $PbCoO_3$ at ambient condition.[15] While Co^{3+} is in the low-spin state, the spin state of Co^{2+} is progressively affected by external pressure, and the high-spin state at ambient pressure (AP) completely transforms into the low-spin state when the pressure reaches 15 GPa. When the pressure is further increased, charge transfer between Pb^{4+} and Co^{2+} occurs between 20 and 30 GPa, resulting in a $Pb^{2+}_{0.5}Pb^{4+}_{0.5}Co^{3+}O_3$ charge distribution. These results suggest the possibility of pressure-induced crystal structure changes and charge transfer transitions in other $PbMO_3$.
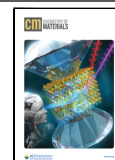
We previously reported that $PbFeO_3$ has a $Pb^{2+}_{0.5}Pb^{4+}_{0.5}Fe^{3+}O_3$ charge distribution with a complex ordering of Pb^{2+} and Pb^{4+} in a $2a_p \times 6a_p \times 2a_p$ superstructure with the $Cmcm$ space group, where a_p is a unit cell of simple perovskite.[11] In this structure, a layer with only Pb^{2+} (A) and layers of ordered Pb^{2+} and Pb^{4+} in a 1:3 ratio (B) are stacked in

an A−B−B−A−B−B sequence along the b-axis.[11] Such ordering of Pb^{2+} and Pb^{4+} generates two inequivalent Fe^{3+} sites with different surroundings, leading to the occurrence of a spin reorientation transition at 418 K despite the absence of magnetic ions other than Fe^{3+}. Similar to $PbCoO_3$ and $PbCrO_3$ mentioned above,[14,16] a pressure-induced charge transfer between Pb and Fe is expected to occur, resulting in a $Pb^{2+}Fe^{4+}O_3$ high-pressure (HP) phase. Such a transition is expected to be accompanied by a huge volume reduction which leads to the development of technologically important new negative thermal expansion materials as seen in the cases of $BiNiO_3$ and $PbVO_3$.[12,20−28]

In this study, $PbFeO_3$ was comprehensively investigated under HP conditions by synchrotron X-ray diffraction (SXRD), Mössbauer spectroscopy, and density functional theory (DFT) calculations. At pressures above 29.0 GPa, $PbFeO_3$ takes a $GdFeO_3$-type orthorhombic $\sqrt{2}a_p \times 2a_p \times \sqrt{2}a_p$ structure with a space group of $Pnma$, in which equivalent Pb and Fe sites are present. The absence of distinct volume shrinkage indicated a $Pb^{2+}_{0.5}Pb^{4+}_{0.5}Fe^{3+}O_3$ charge combination with a glassy distribution of Pb^{2+} and Pb^{4+} in the $Pnma$ phase. The unique Fe^{3+} site was verified by Mössbauer spectroscopy. In addition, the HP structural phase-transition determined by our DFT calculations is in good agreement with the experimental observation. The DFT calculation also confirmed the absence of a charge transfer transition to $Pb^{2+}Fe^{4+}O_3$ up to 70 GPa.

■ EXPERIMENTAL SECTION

Materials Synthesis. Polycrystalline samples $PbFeO_3$ were synthesized using a high-pressure and high-temperature method following the previously reported method.[11]

Characterizations. The HP-SXRD experiment on $PbFeO_3$ was performed at the BL22XU beamline of SPring-8 by using an X-ray wavelength of 0.49594 Å. The sample was loaded into a membrane-driven diamond anvil cell (DAC) with rhenium gasket and He pressure medium using a gas-loading system.[29] The curet size was 350 μm and the sample space was 175 μm diameter and 56 μm height. The ruby fluorescence was used to determine the pressures in this and following HP experiments.[30] The lattice constants were refined using the Le Bail method with the software TOPAS.[31]

HP ^{57}Fe Mössbauer data were acquired at room temperature using a Bassett-type DAC with rhenium gaskets and Daphne 7474 pressure medium.[32] The curet size was 600 μm, and the sample space was 350 μm diameter. ^{57}Co in a Rh matrix was used as the γ-ray source with an output of 1430−1720 MBq and a circular active area having a 4 mm diameter. The velocity scale for each spectrum was determined to be relative to that for α-Fe at room temperature.

HP Raman measurements were conducted at room temperature using a Mao−Bell-type DAC with a rhenium gasket without pressure medium. The curet size was 300 μm, and the sample space was 120 μm diameter and 25 μm height. The Raman spectra were excited using a 785 nm laser and recorded using a HORIBA Evolution Raman microscope. The laser beam spot was about 20−30 μm.

Computational Details. To investigate the ground state structure and associated electronic structure of $PbFeO_3$ as a function of hydrostatic pressure, we performed first-principles calculations based on DFT. To simulate the effect of external pressure, we optimized the atomic positions of $PbFeO_3$ by varying the volume (V) of the system and calculated the corresponding total energies $E(V)$. Then the third-order Birch−Murnaghan isothermal equation of state, given below, was used to estimate the value of the bulk modulus (K_0) and its derivative with respect to pressure (K')

$$E(V) = E_0 + \frac{9V_0K_0}{16}\left\{\left[\left(\frac{V_0}{V}\right)^{2/3} - 1\right]^3 K' + \left[\left(\frac{V_0}{V}\right)^{2/3} - 1\right]^2 \left[6 - 4\left(\frac{V_0}{V}\right)^{2/3}\right]\right\} \quad (1)$$

Here, V_0 represents volume of the system corresponding to the minimum energy.[33] Then the value of pressure associated with each volume for each phase of $PbFeO_3$ was estimated by

$$P(V) = \frac{3K_0}{2}\left[\left(\frac{V_0}{V}\right)^{7/3} - \left(\frac{V_0}{V}\right)^{5/3}\right]\left\{1 + \frac{3}{4}(K' - 4)\left[\left(\frac{V_0}{V}\right)^{2/3} - 1\right]\right\} \quad (2)$$

To calculate $E(V)$, we used the projector augmented plane-wave (PAW) basis method as implemented in the Vienna ab initio simulation package (VASP).[34−36] The revised Perdew−Burke−Ernzerhof form of the generalized gradient approximation (GGA) for solids (PBEsol) was used to calculate the exchange-correlation functional, and the GGA + U method developed by Dudarev et al. was used to describe electron−electron correlation in the Fe 3d state. All calculations were performed with an effective Hubbard parameter U_{eff} = $U - J_H$ = 4.5 eV for the Fe 3d states, where U_{eff} and J_H represent the effective on-site Coulomb and exchange parameter, respectively.[37−39] A kinetic energy cutoff value of 500 eV and appropriate Monkhorst−Pack Γ centered k-point meshes were selected. The equilibrium crystal structure was obtained for each structural phase of $PbFeO_3$ by performing unconstrained optimization of the crystal structure by considering the electronic convergence criterion of 10^{-8} eV and the Hellman−Feynman force convergence criterion of 0.001 eV Å^{-1}. Around the equilibrium crystal structure, we optimized the structural parameters by varying the volume of the system. At each volume, we optimized the structure by keeping the symmetry fixed but by allowing possible change in the shape. We also computed the frequencies of the zone-center and zone-boundary phonon modes for the equilibrium structures of the phases to examine the dynamical instabilities.

To investigate the nature of chemical bonds in various structural phases of $PbFeO_3$, we analyzed crystal orbital Hamiltonian population calculated by using local-orbital basis suite toward electronic-structure reconstruction package.[40] Using this package, the optimized PAW wave functions were projected onto an auxiliary local basis set corresponding to unitary transformation from a delocalized plane wave basis set to a localized Staler-type orbital.[41] Here, the COHP as a function of energy (E) is defined as, $-COHP_{ij}(E) = H_{ij}\sum_n c_i^n{}^* c_j^n \delta(E - E_n)$, where H_{ij} denotes the matrix element between atomic orbitals Φ_i and Φ_j, and c_i^n represents the coefficients associated with Φ_i in a molecular orbital, $\Psi_n = \sum_i c_i^n \Phi_i$. According to the convention, the plus sign is added to plot COHP as a function of E. While $-COHP(E) > 0$ indicates a bonding character between a pair of atomic orbitals, $-COHP(E) < 0$ denotes antibonding interactions. The bonding and antibonding interactions have stabilizing and destabilizing effect on the energy, respectively. If the interaction between atomic orbitals has no impact on the energy and, hence, is a nonbonding character, then $COHP(E) = 0$. Therefore, by analyzing the partial COHP (pCOHP) between two considered atoms one can evaluate if the interaction is bonding, antibonding, or nonbonding. We also calculated the energy integrated COHP up to the Fermi level to evaluate the electronic energy associated with the chemical bond covalency.

We further cross-checked the electronic structure of each structural phase of $PbFeO_3$ by using the full-potential linear augmented plane-wave method as implemented in WIEN2k code with the same value of U_{eff} as we used in VASP calculations.[42] All calculations were performed by using a plane-wave cutoff of RK_{MAX} = 7.5 and a Monkhorst−Pack Γ centered k-point mesh based on the symmetry of the respective structural phase of $PbFeO_3$.

■ RESULTS AND DISCUSSION

Crystal Structure of PbFeO$_3$ under High Pressure.
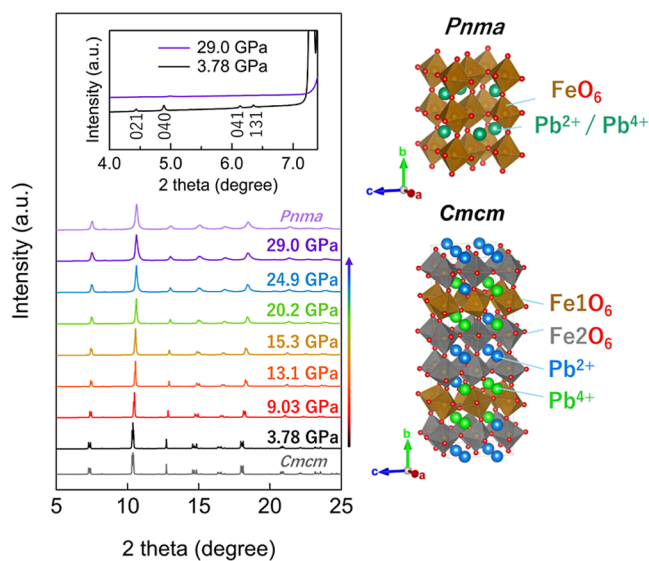Figure 1 shows the results of SXRD experiments at 3.78−29.0

Figure 1. SXRD patterns for PbFeO$_3$ under HP conditions. The inset shows a magnified view around the peaks showing the phase transition. The simulated patterns for the *Cmcm* AP phase are shown at the bottom. Plotted at the top is the result of the Le Bail fitting for the *Pnma* HP phase. The crystal structure of PbFeO$_3$ at AP (*Cmcm*) and HP conditions (*Pnma*) are also shown.[44]

GPa. As pressure increased, the peaks shifted toward the high-angle side overall, indicating continuous decreases in lattice constants and unit-cell volume. However, we did not observe a distinct shift that indicated volume collapse due to the charge transfer transition. In addition to the merging of the peaks, the 021, 040, 041, and 131 peaks disappeared at 29.0 GPa, as shown in Figure 1, suggesting the disappearance of 6-fold periodicity in the *b*-axis.[11,43]

The SXRD pattern at 29.0 GPa can be indexed assuming a $\sqrt{2}a_p \times 2a_p \times \sqrt{2}a_p$ unit cell with the *Pnma* space group (Figure 2). The lattice constants refined by Le Bail fitting are a = 5.3823(5) Å, b = 7.5059(9) Å, and c = 5.3516(2) Å. The HP phase has a GdFeO$_3$-type structure with unique Pb and Fe sites
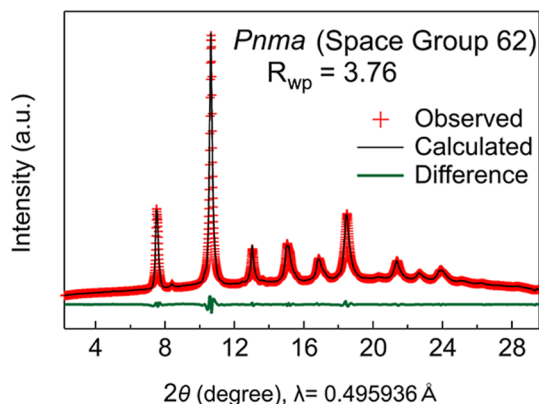

Figure 2. Le Bail fitting results of SXRD data for PbFeO$_3$ at 29.0 GPa[46] showing the observed (red crosses) and calculated (solid black lines) profiles. The solid green lines represent the differences between the two profiles.

and $a^-b^+a^-$ tilting of the FeO$_6$ octahedron. Polar BiInO$_3$-type structure with the space group of $Pn2_1a$ and the same $a^-b^+a^-$ tilting of the FeO$_6$ octahedron is also possible from the extinction rules.[45] Since this structure has unique Pb and Fe sites, our conclusion, pressure-induced amorphization of Pb^{2+}/Pb^{4+} does not change. In addition, BiInO$_3$ transforms into nonpolar *Pnma* phase at 2 GPa.[10] The $Pn2_1a$ phase of PbFeO$_3$ is not expected to be stable at 29.0 GPa. It should be noted that the refinement of the atomic positions and determination of the space group, *Pnma* or $Pn2_1a$, by Rietveld analysis were impossible because of the unreliable intensity ratios due to the limited number of particles in a DAC.

Figure 3 plots the pressure dependence of the lattice parameters and the reduced unit-cell volume. Invisible errors are smaller than the markers. No distinct decrease was observed in both the lattice volume and lattice parameters at the charge glass transition, suggesting the absence of a charge transfer between Pb^{4+} and Fe^{3+} and the preservation of Fe^{3+} in the HP phase. As shown in Figure S1, intensity of 040 peak originating from the 6-fold periodicity in the *b*-axis does not decrease before the sudden disappearance at 29.0 GPa indicating the first order nature of the transition although the lattice constant changes are continuous.

Mössbauer spectroscopy was conducted under pressure to obtain detailed information about the Fe ions. The results are plotted in Figure 4 and the fitting parameters are listed in Table 1. At 3.0 GPa, the spectrum can be fitted with three sets of magnetic sextets, which are attributed to Fe at the 16h and 8d sites shown in green and blue, respectively, and to the α-Fe$_2$O$_3$ impurity shown in pink. This result is consistent with the Fe site ratio of 2:1 in the PbFeO$_3$ crystal structure under ambient conditions. At 23.0 GPa, the impurity-derived magnetic splitting became indistinct, making it impossible to separate from Fe at the 16h sites. We observed an increased proportion of the 16h site in the magnetic splitting pattern. The Mössbauer parameters indicate that the local crystallographic structure of the 8d sites gradually become closer to that of the 16h site as the pressure increases. At 32.5 GPa, the spectra could be fitted with only one set of magnetic sextets. Judging from the isomer shift (IS), Fe remained in the trivalent high-spin state. These results are consistent with our SXRD study, which indicated a GdFeO$_3$-type structure in the HP phase with a unique Fe site. Considering the trivalent nature of Fe ions and the existence of only one crystallographic Pb site, the charge distribution of the HP phase should be Pb$^{2+}_{0.5}$Pb$^{4+}_{0.5}$Fe^{3+}O$_3$ with a glassy distribution of Pb^{2+}/Pb^{4+} as observed in the AP phase of PbCrO$_3$. Interestingly, the glassy distribution of Pb^{2+}/Pb^{4+} in PbCrO$_3$ is absent in the Pb^{2+}Cr^{4+}O$_3$ HP phase, while PbFeO$_3$ exhibits pressure-induced amorphization of Pb^{2+}/Pb^{4+}. Such pressure-induced amorphization has been reported in a wide variety of systems such as AlPO$_4$,[47,48] SnI$_4$,[49] VO$_2$,[50] EuIn$_2$As$_2$,[51] and EuSn$_2$P$_2$[52] and has been a growing area of interest.[53−55]

We also verified the pressure-induced phase transition with Raman spectroscopy under high pressure, as shown in Figure S2. The mode position exhibits a blue shift as the pressure increases, attributed to the reduction in lattice volume. Furthermore, an incremental rise in the phonon width is observed with increasing pressure, which may stem from the effects of strain and changes in particle size induced by HP conditions. Although there is no discernible active mode appearing and disappearing (Figure S2a), when a plot of the active modes with pressure is extracted as in Figure S2b, a
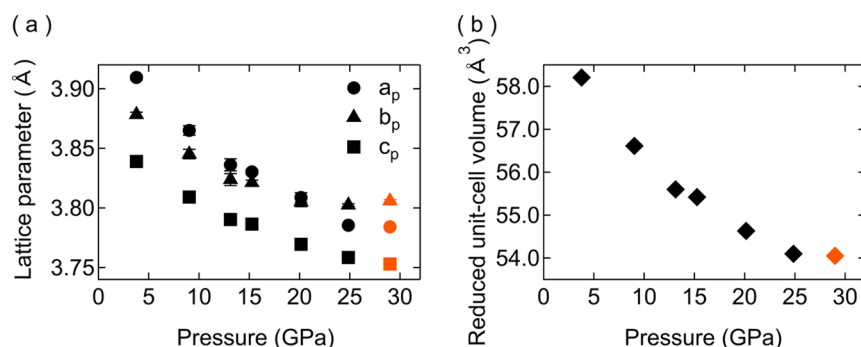
Figure 3. (a) Pressure dependence of the reduced lattice parameters: 1/2 for a (circle) and c (square), 1/6 for b (triangle) for the *Cmcm* (black) and *Pnma* phase (orange). (b) Pressure dependence of the reduced unit-cell volumes: 1/24 for $2a_p \times 6a_p \times 2a_p$ *Cmcm* phase (black) and 1/4 for $\sqrt{2}a_p \times 2a_p \times \sqrt{2}a_p$ *Pnma* phase (orange).
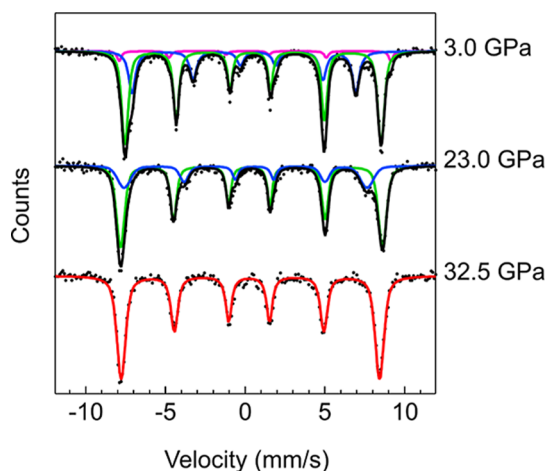

Figure 4. ^{57}Fe Mössbauer spectrum for PbFeO$_3$ at elevated pressures at room temperature.

distinct pressure dependence can be seen in the two phases, which corresponds to the phase transition from the *Cmcm* to *Pnma* phase as determined by SXRD. In addition, we also attempted to conduct the measurement of the electrical transport properties under high pressure. When we used the standard four-wire method in the DAC, we found that the resistance of the sample was $>1 \times 10^6$ Ω, which is beyond the range of the multimeter. Even though the pressure increased to 41 GPa, the magnitude of resistance was still too large to detect. Therefore, the phase transition occurring around 29 GPa is again shown to be independent of charge transfer, where metallic behavior is expected to occur if a transition to HP Pb^{2+}Fe^{4+}O$_3$ phase occurs.

Theoretical Investigation of the Effect of Hydrostatic Pressure. PbFeO$_3$ at AP shows *Cmcm* symmetry that arises out of the condensation of zone-boundary modes involving rigid rotations of oxygen octahedra [R$_4^+$(0, 0, a) and M$_3^+$(a; 0;

0)] and the charge disproportionation in the lead sublattice and subsequent formation of nontrivial long-range charge ordered pattern in the $2a_p \times 6a_p \times 2a_p$ supercell of the cubic $Pm\bar{3}m$ structure. In contrast to the common $a^-b^+a^-$ FeO$_6$ octahedra rotational pattern of the *Pnma* structure, the ground state phase exhibits an $a^+b^-c^+$ rotational pattern. The system also exhibits multiple zone-center and zone-boundary phonon distortions.[11] The crystal structure has two inequivalent Fe sites (8d and 16h) and six inequivalent Pb sites having a 4c Wyckoff label. Figure 5a shows the computed partial DOS and
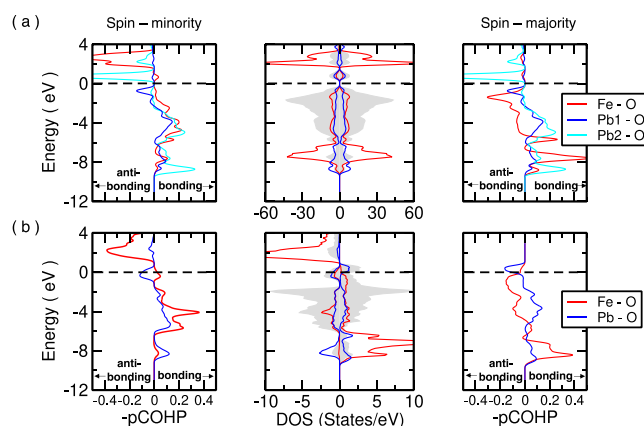

Figure 5. Computed partial density of states (DOS) and COHP for the Fe−O, Pb−O bonds of the ground state *Cmcm* (a) and *Pnma* (b) phase of PbFeO$_3$. The right and left panels denote the computed pCOHP for the spin majority and minority channel, respectively. The partial DOS corresponding to Fe, Pb, and O states are plotted in red, blue, and gray color, respectively.

COHP curves of the insulating *Cmcm* phase of PbFeO$_3$ corresponding to the lowest energy G-type antiferromagnetic (AFM) phase. The Fe ions, being in the high spin state (m_{Fe} ~4.2 μB) in the majority spin channel the Fe−O pd bonding

Table 1. Fitting Parameters of ^{57}Fe Mössbauer Spectrum

	line color	IS (mm/s)	QS (mm/s)	B_{hf} (T)	Γ (mm/s)	ΔB (T)	area (%)
3.0 GPa	green (16h)	0.40	0.17	49.8	0.36	0.7	63.0
	blue (8d)	0.36	−0.89	43.5	0.50	0.0	32.3
	pink (α-Fe$_2$O$_3$)	0.38	0.47	52.9	0.30	0.0	4.7
23.0 GPa	green (16h)	0.32	0.14	51.0	0.35	1.0	71.7
	blue (8d)	0.30	−0.57	47.3	0.39	2.0	28.3
32.5 GPa	red (4c, *Pnma*)	0.28	0.08	50.3	0.43	1.0	100

states with predominantly Fe−3d orbital character are occupied and are well separated (∼10 eV) from the corresponding unoccupied antibonding states are in the minority spin channel. The Fe−O bonding and antibonding states primarily formed of the oxygen p orbitals lie within an energy window of ∼6 eV below the Fermi level. Therefore, in the ground state crystal structure, the Fe ions are expected to form d^5 electronic configurations. Two different types of Pb ions are observed here, namely Pb1 and Pb2. The computed COHP between the orbitals of Pb and oxygen atoms show that in the case of Pb1, both bonding and antibonding sp states are occupied, indicating the formation of $6s^2$ electronic configuration with nominal valence state of 2+ ($6s^{2.02}$, according to Mulliken population analysis). Pb1 6s orbitals form weak covalent bonds with the oxygen p orbitals. On the other hand, the covalency between the Pb2 6s and oxygen 2p orbitals was found to be significantly stronger as shown in Figure 5a. In both the majority and minority spin channels, the lowest energy conduction band is formed by Pb2−O sp* antibonding states with strong hybridization with the oxygen p orbitals, while the Pb2−O sp bonding states having Pb 6s character are occupied and well separated from the sp* states. This indicates the formation of the $6s^2\underline{L}^2$ configuration ($6s^{1.34}$, according to Mulliken population analysis), where $\underline{L}$ denotes ligand hole, as has been observed in various lead and bismuth based oxide materials.[56−58] The ligand holes are, therefore, localized in the Pb2−O bonds. We denote these Pb ions as Pb^{4+}.

Compared to this ground state structure, the cubic $Pm\overline{3}m$ and orthorhombic $Pnma$ phases are 0.82 and 0.14 eV/f.u. higher in energy, respectively. The $Pnma$ phase without charge disproportionation is metallic in nature (see Figure 5b). From the computed DOS (see Figure 5b), we observe that similar to $Cmcm$ phase, the Fe ions form high spin state having t_{2g} and e_g states almost occupied and empty in the majority and minority spin channels, respectively, forming $d^5\underline{L}^\delta$ configuration, where value of δ is negligibly small. In the proximity of the Fermi level, under the influence of the Pb−O bonds, the states assume antibonding sp* character. Formation of these antibonding states indicates the $6s^2\underline{L}^{1-\delta}$ electronic configuration ($6s^{1.74}$, according to Mulliken population analysis) of the Pb ions where the ligand holes are delocalized in the Pb−O covalent bond. This is in sharp contrast to ferrite perovskite with divalent A-site cations, such as $CaFeO_3$ and $BaFeO_3$.[59,60] In case of $Pnma$ phase of $CaFeO_3$ (see Figure S3), the Fermi level falls in a Fe−O pd* antibonding states strongly hybridized with the oxygen p orbitals. The presence of such antibonding states at the Fermi level may lead to the charge disproportionation in the Fe sublattice [Fe^{3+} (d^5) and Fe^{5+} $d^5\underline{L}^2$], as was reported.[61] Similarly, in case of $BaFeO_3$, formation of ligand hole delocalized in the Fe−O bond of the cubic $Pm\overline{3}m$ phase was also reported, which was found to have significant impact on the defect formation.[62] It is also noteworthy in this context that the electronic structure of $Pnma$ phase of $PbFeO_3$ is significantly different from that in case of $BiNiO_3$ (Figure S4), which exhibits pressure induced charge transfer transition.[10] While in the case of $BiNiO_3$, the states crossing the Fermi level have predominantly Ni−O pd* antibonding character, in the case of $PbFeO_3$, the same have Pb−O sp* antibonding character. Therefore, transition to the orthorhombic $Pnma$ phase in $PbFeO_3$, in contrast to the similar transition in $BiNiO_3$, is not expected to change the character of ligand hole from Pb−O to Fe−O.[10] This mismatch can be attributed to the influence of the half-filled

electron occupancy of the Fe 3d states and the strong covalency between lead and oxygen ions in the latter system.

Formation of large antibonding states near the Fermi level may lead to structural distortions forming lower-symmetry phases. The $Pnma$ phase was indeed found to be dynamically unstable with phonon modes having imaginary frequencies at both the zone center (Γ) and the zone boundary k-points. Interestingly, the phonon modes with high imaginary frequencies drive layered arrangements between Pb^{2+} and Pb^{4+} type ions. The long-range charge ordered state along the q_1 (crystallographic [010] axis) propagation vector (C_{q_1}) has noncentrosymmetric space group $Pmc2_1$ (see Figure S5a) associated with the structural distortion having Γ_3^- irreducible representation. The $Pmc2_1$ phase exhibits layered ordering along the crystallographic [010] axis. On the other hand, the structural distortions at $U\left(\frac{1}{2}, 0, \frac{1}{2}\right)$ with U_1^+ U_4^+ irreducible representation leads to the centrosymmetric charge ordered state having $P2_1/m$ symmetry. The Pb^{2+}/Pb^{4+} ordered states, as depicted in Figure S5b,c, having q_2 (crystallographic [101] axis) and q_3 (crystallographic [10−1] axis) propagation vectors being energetically equivalent, form a charge frustration in the crystallographic (010) plane. Nontrivial layered structures driven by the structural instabilities at the Y (0, 1/2, 0) and DT (0, 1/3, 0) k-points exhibit $L_{Pb^{2+}} - L_{Pb^{2+}} - L_{Pb^{4+}} - L_{Pb^{4+}}$ (C_{qY}) and $L_{Pb^{2+}} - L_{Pb^{4+}} - L_{RS} - L_{Pb^{2+}} - L_{Pb^{4+}} - L_{RS}$ (C_{qDT}) type patterns, respectively, along the crystallographic [010] axis. Where $L_{Pb^{2+}}$ and $L_{Pb^{4+}}$ denote layers containing Pb^{2+} and Pb^{4+} ions, respectively. Moreover, in the L_{RS} layer, the Pb^{2+} and Pb^{4+} ions are ordered in rock-salt pattern. The calculated energy of these identified phases as a function of volume is shown in Figure 6a. Among the layered phases, the most stable configuration has Pc symmetry with C_{qY} charge pattern compared to which the C_{qDT} state is only 3 meV/f.u. higher in energy. Several layered states lie within ∼20 meV/f.u. energy window. We also have observed that $L_{Pb^{4+}} - L_{Pb^{4+}} - L_{Pb^{2+}} - L_{Pb^{4+}} - L_{Pb^{4+}} - L_{Pb^{2+}}$ type charge pattern along the [010] axis with metallic solution that leads
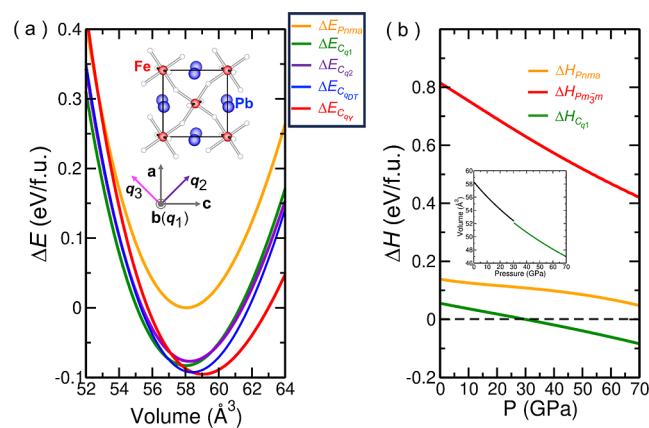

Figure 6. (a) Computed relative energy of the various layered charge ordered phases within the $a^-b^+a^-$ FeO_6 octahedra rotational framework. (b) Computed relative enthalpy of various phases of $PbFeO_3$ as a function of pressure with respect to the ground state $Cmcm$ structure. The estimated bulk modulus (K_0 ∼170 GPa) of $PbFeO_3$ does not vary significantly, depending on the structural phase. We calculated the energies as a function of volume by optimizing the structure with symmetry and volume fixed. The inset shows change of volume as a function of pressure.

to the creation of mixed valent Fe ions is ~48 meV/f.u. higher in energy compared to most stable layered charge ordered state. Our detailed investigations pointed toward the following key characteristics of the orthorhombic $Pnma$ phase, (1) tendency of charge disproportionation in the lead sublattice with 1:1 ratio which stabilize the d^5 electronic configuration of Fe ions, (2) high probability of formation of charge disordered phase at finite temperature as various competing charge ordered phases lie close to the most stable structure. The preference of layered ordering over other common charge ordered phases, such as rock-salt and columnar, is expected to be contributed by the d^5 electronic configuration of the Fe ions which display antiferroelectric type displacements in all the layered phases (see Figure S5). Compared to the most stable layered phase, the rock-salt and the columnar phases (Figure S6) are ~12 and ~54 meV/f.u. higher in energy, respectively. The presence of energetically competing long-range ordered phases in PbFeO$_3$ bears a likely relation with the strong cation−anion hybridization and high stiffness constant of the corresponding bonds in the PbFeO$_3$, as was discussed in ref 63.

Finally, we investigated the stability of the ground state structure as a function of external pressure ranging from 0 to 70 GPa, the results of which are summarized in Figure 6b. We optimized the structural phases by taking into account the G-type AFM order of the Fe spins as was detected in the previous study.[11] As can be clearly observed from Figure 6b, we did not observe any charge transfer transition associated with the transfer of ligand holes from the Pb−O to Fe−O bonds. Here, it is worthwhile to mention that the transition from the ambient pressure phase to the cubic $Pm\overline{3}m$ phase (see Figure S7) can lead to partial charge transfer from Pb−O sp* → Fe−O pd* antibonding state. However, according to our results, the system did not transit to the cubic phase even at a high pressure of 70 GPa. Instead, a change in the oxygen octahedral rotational pattern from $a^+b^-c^+ \rightarrow a^-b^+a^-$ was observed at P_c ~30 GPa, which was in good agreement with experiment. All of the layered phases are insulating in nature in contrast to the metallic $Pm\overline{3}m$ phase. This phase above ~30 GPa shows the formation of charge disproportionation in the lead sublattice and is associated with just a small reduction in volume (~0.5%), which is in good agreement with the experiment (see Figure 6b). DFT calculations were performed considering layered charge ordered phases with an $a^-b^+a^-$ rotational pattern. However, as it has been experimentally observed, at finite temperature the charge amorphization is more likely to occur. However, it should be noted that during the phase transition, we observed a corresponding change in the oxygen octahedral rotational pattern instead of any transfer of charge. This, however, is in contrast to our observation in other Pb-based perovskite oxides.

The phase diagram of PbFeO$_3$ constructed based on our experimental and theoretical investigations is compared with that of PbCrO$_3$ in Figure 7. The behavior of PbFeO$_3$ is in contrast to that of PbCrO$_3$, where the melting of charge glass and simultaneous Pb−Cr charge transfer take place under the HP condition, indicating that such a glassy distribution of charges is sensitive to external stimuli. The charge combination Pb$^{2+}_{0.5}$Pb$^{4+}_{0.5}$Fe^{3+}O$_3$ with a glassy distribution of Pb^{2+} and Pb^{4+} is expected to change into the Pb^{2+}Fe^{4+}O$_3$ state at higher pressure, but our DFT calculations indicated the absence of a charge-transfer transition below 70 GPa. An even higher pressure is necessary to observe the transition to the Pb^{2+}Fe^{4+}O$_3$ phase.
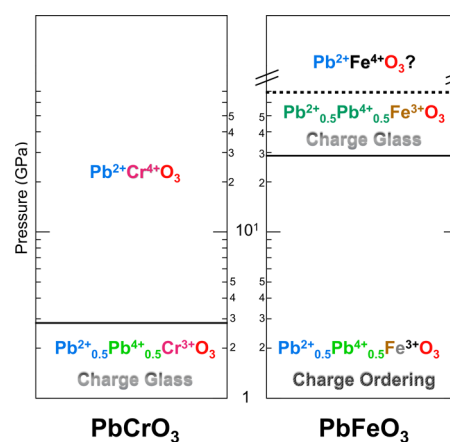

Figure 7. Phase diagram of PbCrO$_3$ and PbFeO$_3$ at room temperature.

■ SUMMARY

We investigated the HP behavior of perovskite oxide PbFeO$_3$ with Pb$^{2+}_{0.5}$Pb$^{4+}_{0.5}$Fe^{3+}O$_3$ charge distribution and complex ordering of Pb^{2+} and Pb^{4+} and two Fe^{3+} sites at AP. HP-SXRD and Mössbauer and Raman spectroscopies revealed a pressure-induced structural phase transition at 29.0 GPa to an orthorhombic GdFeO$_3$-type structure with a glassy distribution of Pb^{2+} and Pb^{4+} and a unique Fe^{3+} site, namely, pressure induced amorphization of Pb^{2+} and Pb^{4+}. Further change into the Pb^{2+}Fe^{4+}O$_3$ state is expected at higher pressure, but our DFT calculations indicated the absence of a charge−transfer transition below 70 GPa.

■ ASSOCIATED CONTENT

Ⓢ Supporting Information

The Supporting Information is available free of charge at https://pubs.acs.org/doi/10.1021/acs.chemmater.3c02569.

Pressure dependence of the intensity of 040 peak; HP-Raman data; computed partial density of states (DOS) and COHP; and structural models for computations (PDF)

■ AUTHOR INFORMATION

Corresponding Authors

Qiumin Liu − *Laboratory for Materials and Structures, Tokyo Institute of Technology, Yokohama 226-8501, Japan;* Email: liu.q.ae@m.titech.ac.jp

Hena Das − *Laboratory for Materials and Structures, Tokyo Institute of Technology, Yokohama 226-8501, Japan; Kanagawa Institute of Industrial Science and Technology, Ebina 243-0435, Japan;* ⓞ orcid.org/0000-0001-5378-066X; Email: das.h.aa@m.titech.ac.jp

Masaki Azuma − *Laboratory for Materials and Structures, Tokyo Institute of Technology, Yokohama 226-8501, Japan; Kanagawa Institute of Industrial Science and Technology, Ebina 243-0435, Japan; Living Systems Materiology Research (LiSM) Group, International Research Frontiers Initiative (IRFI), Tokyo Institute of Technology, Yokohama 226-8501, Japan;* ⓞ orcid.org/0000-0002-8378-321X; Email: mazuma@msl.titech.ac.jp

Authors

Takumi Nishikubo − *Laboratory for Materials and Structures, Tokyo Institute of Technology, Yokohama 226-*

8501, Japan; Kanagawa Institute of Industrial Science and Technology, Ebina 243-0435, Japan; ⊚ orcid.org/0000-0002-1250-3057

Yuki Sakai − *Laboratory for Materials and Structures, Tokyo Institute of Technology, Yokohama 226-8501, Japan; Kanagawa Institute of Industrial Science and Technology, Ebina 243-0435, Japan;* ⊚ orcid.org/0000-0002-8427-4740

Ko Mibu − *Department of Physical Science and Engineering, Nagoya Institute of Technology, Nagoya 466-8555, Japan;* ⊚ orcid.org/0000-0002-6416-1028

Tomoko Onoue − *Department of Physical Science and Engineering, Nagoya Institute of Technology, Nagoya 466-8555, Japan*

Takateru Kawakami − *Department of Physics, College of Humanities and Sciences, Nihon University, Tokyo 156-8550, Japan*

Tetsu Watanuki − *Synchrotron Radiation Research Center, National Institutes for Quantum Science and Technology (QST), Sayo-gun, Hyogo 679-5148, Japan*

Akihiko Machida − *Synchrotron Radiation Research Center, National Institutes for Quantum Science and Technology (QST), Sayo-gun, Hyogo 679-5148, Japan*

Xubin Ye − *Beijing National Laboratory for Condensed Matter Physics, Institute of Physics, Chinese Academy of Sciences, Beijing 100190, China;* ⊚ orcid.org/0000-0002-5739-8318

Jianhong Dai − *Beijing National Laboratory for Condensed Matter Physics, Institute of Physics, Chinese Academy of Sciences, Beijing 100190, China*

Zhao Pan − *Laboratory for Materials and Structures, Tokyo Institute of Technology, Yokohama 226-8501, Japan; Present Address: Beijing National Laboratory for Condensed Matter Physics, Institute of Physics, Chinese Academy of Sciences, Beijing 100190, China;* ⊚ orcid.org/0000-0002-8693-2508

Lei Hu − *Laboratory for Materials and Structures, Tokyo Institute of Technology, Yokohama 226-8501, Japan; Present Address: Material Science and Engineering, Xi'an Jiaotong University, Xi'an 710049, China.;* ⊚ orcid.org/0000-0002-4647-1604

Satoshi Nakano − *National Institute for Materials Science, Tsukuba, Ibaraki 305-0044, Japan;* ⊚ orcid.org/0000-0002-7010-9867

Masayuki Fukuda − *Laboratory for Materials and Structures, Tokyo Institute of Technology, Yokohama 226-8501, Japan; Present Address: Advanced Manufacturing Research Institute, National Institute of Advanced Industrial Science and Technology, Tsukuba Central 5, 1-1-1 Higashi, Tsukuba, Ibaraki 305-8565, Japan.;* ⊚ orcid.org/0000-0002-3153-9602

Shiori Kihara − *Laboratory for Materials and Structures, Tokyo Institute of Technology, Yokohama 226-8501, Japan*

Koomok Lee − *Laboratory for Materials and Structures, Tokyo Institute of Technology, Yokohama 226-8501, Japan*

Takehiro Koike − *Laboratory for Materials and Structures, Tokyo Institute of Technology, Yokohama 226-8501, Japan;* ⊚ orcid.org/0000-0002-3588-6708

Youwen Long − *Beijing National Laboratory for Condensed Matter Physics, Institute of Physics, Chinese Academy of Sciences, Beijing 100190, China; University of Chinese Academy of Sciences, Beijing 100049, China; Songshan Lake*

Materials Laboratory, Dongguan, Guangdong 523808, China; ⊚ orcid.org/0000-0002-8587-7818

Complete contact information is available at:
https://pubs.acs.org/10.1021/acs.chemmater.3c02569

Notes
The authors declare no competing financial interest.

REFERENCES

(1) Dagotto, E.; Hotta, T.; Moreo, A. Colossal magnetoresistant materials: the key role of phase separation. *Phys. Rep.* **2001**, *344* (1−3), 1−153.

(2) Salamon, M. B.; Jaime, M. The Physics of Manganites: Structure and Transport. *Rev. Mod. Phys.* **2001**, *73* (3), 583−628.

(3) Imada, M.; Fujimori, A.; Tokura, Y. Metal-Insulator Transitions. *Rev. Mod. Phys.* **1998**, *70* (4), 1039−1263.

(4) Keimer, B.; Kivelson, S. A.; Norman, M. R.; Uchida, S.; Zaanen, J. From Quantum Matter to High-Temperature Superconductivity in Copper Oxides. *Nature* **2015**, *518* (7538), 179−186.

(5) Niitaka, S.; Azuma, M.; Takano, M.; Nishibori, E.; Takata, M.; Sakata, M. Crystal Structure and Dielectric and Magnetic Properties of $BiCrO_3$ as a Ferroelectromagnet. *Solid State Ionics* **2004**, *172* (1−4), 557−559.

(6) Naka, M.; Seo, H.; Motome, Y. Theory of Valence Transition in $BiNiO_3$. *Phys. Rev. Lett.* **2016**, *116* (5), 056402.

(7) Belik, A. A.; Iikubo, S.; Kodama, K.; Igawa, N.; Shamoto, S.; Niitaka, S.; Azuma, M.; Shimakawa, Y.; Takano, M.; Izumi, F.; Takayama-Muromachi, E. Neutron Powder Diffraction Study on the Crystal and Magnetic Structures of $BiCoO_3$. *Chem. Mater.* **2006**, *18* (3), 798−803.

(8) Harrison, W. A. Valence-Skipping Compounds as Positive-U Electronic Systems. *Phys. Rev. B: Condens. Matter Mater. Phys.* **2006**, *74* (24), 245128.

(9) Ishiwata, S.; Azuma, M.; Takano, M.; Nishibori, E.; Takata, M.; Sakata, M.; Kato, K. High Pressure Synthesis, Crystal Structure and Physical Properties of a New Ni(II) Perovskite $BiNiO_3$. *J. Mater. Chem.* **2002**, *12* (12), 3733−3737.

(10) Azuma, M.; Carlsson, S.; Rodgers, J.; Tucker, M. G.; Tsujimoto, M.; Ishiwata, S.; Isoda, S.; Shimakawa, Y.; Takano, M.; Attfield, J. P. Pressure-Induced Intermetallic Valence Transition in $BiNiO_3$. *J. Am. Chem. Soc.* **2007**, *129* (46), 14433−14436.

(11) Ye, X.; Zhao, J.; Das, H.; Sheptyakov, D.; Yang, J.; Sakai, Y.; Hojo, H.; Liu, Z.; Zhou, L.; Cao, L.; Nishikubo, T.; Wakazaki, S.; Dong, C.; Wang, X.; Hu, Z.; Lin, H. J.; Chen, C. Te; Sahle, C.; Efiminko, A.; Cao, H.; Calder, S.; Mibu, K.; Kenzelmann, M.; Tjeng, L. H.; Yu, R.; Azuma, M.; Jin, C.; Long, Y. Observation of Novel Charge Ordering and Spin Reorientation in Perovskite Oxide PbFeO₃. *Nat. Commun.* **2021**, *12* (1), 1917.

(12) Azuma, M.; Chen, W. T.; Seki, H.; Czapski, M.; Olga, S.; Oka, K.; Mizumaki, M.; Watanuki, T.; Ishimatsu, N.; Kawamura, N.; Ishiwata, S.; Tucker, M. G.; Shimakawa, Y.; Attfield, J. P. Colossal Negative Thermal Expansion in BiNiO₃ Induced by Intermetallic Charge Transfer. *Nat. Commun.* **2011**, *2* (1), 347.

(13) Shpanchenko, R. V.; Chernaya, V. V.; Tsirlin, A. A.; Chizhov, P. S.; Sklovsky, D. E.; Antipov, E. V.; Khlybov, E. P.; Pomjakushin, V.; Balagurov, A. M.; Medvedeva, J. E.; Kaul, E. E.; Geibel, C. Synthesis, Structure, and Properties of New Perovskite PbVO₃. *Chem. Mater.* **2004**, *16* (17), 3267–3273.

(14) Yu, R.; Hojo, H.; Watanuki, T.; Mizumaki, M.; Mizokawa, T.; Oka, K.; Kim, H.; Machida, A.; Sakaki, K.; Nakamura, Y.; Agui, A.; Mori, D.; Inaguma, Y.; Schlipf, M.; Rushchanskii, K. Z.; Ležaić, M.; Matsuda, M.; Ma, J.; Calder, S.; Isobe, M.; Ikuhara, Y.; Azuma, M. Melting of Pb Charge Glass and Simultaneous Pb–Cr Charge Transfer in PbCrO₃ as the Origin of Volume Collapse. *J. Am. Chem. Soc.* **2015**, *137* (39), 12719–12728.

(15) Sakai, Y.; Yang, J.; Yu, R.; Hojo, H.; Yamada, I.; Miao, P.; Lee, S.; Torii, S.; Kamiyama, T.; Ležaić, M.; Bihlmayer, G.; Mizumaki, M.; Komiyama, J.; Mizokawa, T.; Yamamoto, H.; Nishikubo, T.; Hattori, Y.; Oka, K.; Yin, Y.; Dai, J.; Li, W.; Ueda, S.; Aimi, A.; Mori, D.; Inaguma, Y.; Hu, Z.; Uozumi, T.; Jin, C.; Long, Y.; Azuma, M. A-Site and B-Site Charge Orderings in an s-d Level Controlled Perovskite Oxide PbCoO₃. *J. Am. Chem. Soc.* **2017**, *139* (12), 4574–4581.

(16) Liu, Z.; Sakai, Y.; Yang, J.; Li, W.; Liu, Y.; Ye, X.; Qin, S.; Chen, J.; Agrestini, S.; Chen, K.; Liao, S.-C.; Haw, S.-C.; Baudelet, F.; Ishii, H.; Nishikubo, T.; Ishizaki, H.; Yamamoto, T.; Pan, Z.; Fukuda, M.; Ohashi, K.; Matsuno, K.; Machida, A.; Watanuki, T.; Kawaguchi, S. I.; Arevalo-Lopez, A. M.; Jin, C.; Hu, Z.; Attfield, J. P.; Azuma, M.; Long, Y. Sequential Spin State Transition and Intermetallic Charge Transfer in PbCoO₃. *J. Am. Chem. Soc.* **2020**, *142* (12), 5731–5741.

(17) Inaguma, Y.; Tanaka, K.; Tsuchiya, T.; Mori, D.; Katsumata, T.; Ohba, T.; Hiraki, K.; Takahashi, T.; Saitoh, H. Synthesis, Structural Transformation, Thermal Stability, Valence State, and Magnetic and Electronic Properties of PbNiO₃ with Perovskite- and LiNbO₃-Type Structures. *J. Am. Chem. Soc.* **2011**, *133* (42), 16920–16929.

(18) Belik, A. A.; Azuma, M.; Saito, T.; Shimakawa, Y.; Takano, M. Crystallographic Features and Tetragonal Phase Stability of PbVO₃, a New Member of PbTiO₃ Family. *Chem. Mater.* **2005**, *17* (2), 269–273.

(19) Oka, K.; Azuma, M.; Chen, W. T.; Yusa, H.; Belik, A. A.; Takayama-Muromachi, E.; Mizumaki, M.; Ishimatsu, N.; Hiraoka, N.; Tsujimoto, M.; Tucker, M. G.; Attfield, J. P.; Shimakawa, Y. Pressure-Induced Spin-State Transition in BiCoO₃. *J. Am. Chem. Soc.* **2010**, *132* (27), 9438–9443.

(20) Nabetani, K.; Muramatsu, Y.; Oka, K.; Nakano, K.; Hojo, H.; Mizumaki, M.; Agui, A.; Higo, Y.; Hayashi, N.; Takano, M.; Azuma, M. Suppression of Temperature Hysteresis in Negative Thermal Expansion Compound BiNi₁₋ₓFeₓO₃ and Zero-Thermal Expansion Composite. *Appl. Phys. Lett.* **2015**, *106* (6), 061912.

(21) Oka, K.; Nabetani, K.; Sakaguchi, C.; Seki, H.; Czapski, M.; Shimakawa, Y.; Azuma, M. Tuning Negative Thermal Expansion in Bi₁₋ₓLnₓNiO₃ (Ln = La, Nd, Eu, Dy). *Appl. Phys. Lett.* **2013**, *103* (6), 061909.

(22) Nishikubo, T.; Sakai, Y.; Oka, K.; Mizumaki, M.; Watanuki, T.; Machida, A.; Maejima, N.; Ueda, S.; Mizokawa, T.; Azuma, M. Optimized Negative Thermal Expansion Induced by Gradual Intermetallic Charge Transfer in Bi₁₋ₓSbₓNiO₃. *Appl. Phys. Express* **2018**, *11* (6), 061102.

(23) Nakano, K.; Oka, K.; Watanuki, T.; Mizumaki, M.; Machida, A.; Agui, A.; Kim, H.; Komiyama, J.; Mizokawa, T.; Nishikubo, T.; Hattori, Y.; Ueda, S.; Sakai, Y.; Azuma, M. Glassy Distribution of

Bi³⁺/Bi⁵⁺ in Bi₁₋ₓPbₓNiO₃ and Negative Thermal Expansion Induced by Intermetallic Charge Transfer. *Chem. Mater.* **2016**, *28* (17), 6062–6067.

(24) Sakai, Y.; Nishikubo, T.; Ogata, T.; Ishizaki, H.; Imai, T.; Mizumaki, M.; Mizokawa, T.; MacHida, A.; Watanuki, T.; Yokoyama, K.; Okimoto, Y.; Koshihara, S. Y.; Das, H.; Azuma, M. Polar-Nonpolar Phase Transition Accompanied by Negative Thermal Expansion in Perovskite-Type Bi₁₋ₓPbₓNiO₃. *Chem. Mater.* **2019**, *31* (13), 4748–4758.

(25) Nishikubo, T.; Sakai, Y.; Oka, K.; Watanuki, T.; Machida, A.; Mizumaki, M.; Maebayashi, K.; Imai, T.; Ogata, T.; Yokoyama, K.; Okimoto, Y.; Koshihara, S. Y.; Hojo, H.; Mizokawa, T.; Azuma, M. Enhanced Negative Thermal Expansion Induced by Simultaneous Charge Transfer and Polar-Nonpolar Transitions. *J. Am. Chem. Soc.* **2019**, *141* (49), 19397–19403.

(26) Yamamoto, H.; Imai, T.; Sakai, Y.; Azuma, M. Colossal Negative Thermal Expansion in Electron-Doped PbVO₃ Perovskites. *Angew. Chem.* **2018**, *130* (27), 8302–8305.

(27) Ogata, T.; Oka, K.; Azuma, M. Negative Thermal Expansion in Electron Doped PbVO₃₋ₓFₓ. *Appl. Phys. Express* **2019**, *12* (2), 023005.

(28) Nishikubo, T.; Imai, T.; Sakai, Y.; Mizumaki, M.; Kawaguchi, S.; Oshime, N.; Shimada, A.; Sugawara, K.; Ohwada, K.; Machida, A.; Watanuki, T.; Kurushima, K.; Mori, S.; Mizokawa, T.; Azuma, M. Polar-Nonpolar Transition-Type Negative Thermal Expansion with 11.1% Volume Shrinkage by Design. *Chem. Mater.* **2023**, *35* (3), 870–878.

(29) Kenichi, T.; Sahu, P. Ch.; Yoshiyasu, K.; Yasuo, T. Versatile Gas-Loading System for Diamond-Anvil Cells. *Rev. Sci. Instrum.* **2001**, *72* (10), 3873–3876.

(30) Mao, H. K.; Xu, J.; Bell, P. M. Calibration of the Ruby Pressure Gauge to 800 Kbar under Quasi-Hydrostatic Conditions. *J. Geophys. Res.* **1986**, *91* (B5), 4673–4676.

(31) Coelho, A. A. TOPAS and TOPAS-Academic: an optimization program integrating computer algebra and crystallographic objects written in C++. *J. Appl. Crystallogr.* **2018**, *51* (1), 210–218.

(32) Bassett, W. A.; Takahashi, T.; Stook, P. W. X-Ray Diffraction and Optical Observations on Crystalline Solids up to 300 Kbar. *Rev. Sci. Instrum.* **1967**, *38* (1), 37–42.

(33) Birch, F. Elasticity and Constitution of the Earth's Interior. *J. Geophys. Res.* **1952**, *57* (2), 227–286.

(34) Kresse, G.; Hafner, J. Ab Initio Molecular Dynamics for Liquid Metals. *Phys. Rev. B: Condens. Matter Mater. Phys.* **1993**, *47* (1), 558–561.

(35) Kresse, G.; Furthmüller, J. Efficient Iterative Schemes for Ab Initio Total-Energy Calculations Using a Plane-Wave Basis Set. *Phys. Rev. B: Condens. Matter Mater. Phys.* **1996**, *54* (16), 11169.

(36) Kresse, G.; Furthmüller, J. Efficiency of Ab-Initio Total Energy Calculations for Metals and Semiconductors Using a Plane-Wave Basis Set. *Comput. Mater. Sci.* **1996**, *6* (1), 15–50.

(37) Anisimov, V. I.; Aryasetiawan, F.; Lichtenstein, A. I. First-Principles Calculations of the Electronic Structure and Spectra of Strongly Correlated Systems: The LDA+ U Method. *J. Phys.: Condens. Matter* **1997**, *9* (4), 767.

(38) Dudarev, S. L.; Botton, G. A.; Savrasov, S. Y.; Humphreys, C. J.; Sutton, A. P. Electron-energy-loss spectra and the structural stability of nickel oxide: An LSDA+U study. *Phys. Rev. B: Condens. Matter Mater. Phys.* **1998**, *57* (3), 1505–1509.

(39) Perdew, J. P.; Ruzsinszky, A.; Csonka, G. I.; Vydrov, O. A.; Scuseria, G. E.; Constantin, L. A.; Zhou, X.; Burke, K. Restoring the Density-Gradient Expansion for Exchange in Solids and Surfaces. *Phys. Rev. Lett.* **2008**, *100* (13), 136406.

(40) Maintz, S.; Deringer, V. L.; Tchougréeff, A. L.; Dronskowski, R. LOBSTER: A Tool to Extract Chemical Bonding from Plane-Wave Based DFT. *J. Comput. Chem.* **2016**, *37* (11), 1030–1035.

(41) Davenport, J. W. Linear Augmented-Slater-Type-Orbital Method for Electronic-Structure Calculations. *Phys. Rev. B: Condens. Matter Mater. Phys.* **1984**, *29* (6), 2896–2904.

(42) Schwarz, K.; Blaha, P.; Madsen, G. K. H. Electronic Structure Calculations of Solids Using the WIEN2k Package for Material Sciences. *Comput. Phys. Commun.* **2002**, *147* (1−2), 71−76.

(43) Tsuchiya, T.; Saito, H.; Yoshida, M.; Katsumata, T.; Ohba, T.; Inaguma, Y.; Tsurui, T.; Shikano, M. High-Pressure Synthesis of a Novel PbFeO₃. *MRS Online Proc. Libr.* **2006**, *988* (1), 9880916.

(44) Momma, K.; Izumi, F. VESTA 3 for Three-Dimensional Visualization of Crystal, Volumetric and Morphology Data. *J. Appl. Crystallogr.* **2011**, *44* (6), 1272−1276.

(45) Belik, A. A.; Stefanovich, S. Y.; Lazoryak, B. I.; Takayama-Muromachi, E. BiInO₃: A Polar Oxide with GdFeO₃-Type Perovskite Structure. *Chem. Mater.* **2006**, *18*, 1964−1968.

(46) Hammersley, A. P.; Svensson, S. O.; Hanfland, M.; Fitch, A. N.; Hausermann, D. Two-Dimensional Detector Software: From Real Detector to Idealised Image or Two-Theta Scan. *High Pressure Res.* **1996**, *14* (4−6), 235−248.

(47) Tse, J. S.; Klug, D. D. Structural Memory in Pressure-Amorphized AlPO₄. *Science* **1992**, *255* (5051), 1559−1561.

(48) Sankaran, H.; Sharma, S. M.; Sikka, S. K.; Chidambaram, R. Pressure Induced Amorphization of AlPO₄. *Pramana* **1990**, *35* (2), 177−180.

(49) Liu, H.; Tse, J. S.; Hu, M. Y.; Bi, W.; Zhao, J.; Alp, E. E.; Pasternak, M.; Taylor, R. D.; Lashley, J. C. Mechanisms for Pressure-Induced Crystal-Crystal Transition, Amorphization, and Devitrification of SnI₄. *J. Chem. Phys.* **2015**, *143* (16), 064501.

(50) Wang, Y.; Zhu, J.; Yang, W.; Wen, T.; Pravica, M.; Liu, Z.; Hou, M.; Fei, Y.; Kang, L.; Lin, Z.; Jin, C.; Zhao, Y. Reversible Switching between Pressure-Induced Amorphization and Thermal-Driven Recrystallization in VO₂(B) Nanosheets. *Nat. Commun.* **2016**, *7* (1), 12214.

(51) Yu, F. H.; Mu, H. M.; Zhuo, W. Z.; Wang, Z. Y.; Wang, Z. F.; Ying, J. J.; Chen, X. H. Elevating the Magnetic Exchange Coupling in the Compressed Antiferromagnetic Axion Insulator Candidate EuIn₂As₂. *Phys. Rev. B* **2020**, *102* (18), 180404.

(52) Bi, W.; Culverhouse, T.; Nix, Z.; Xie, W.; Tien, H. J.; Chang, T. R.; Dutta, U.; Zhao, J.; Lavina, B.; Alp, E. E.; Zhang, D.; Xu, J.; Xiao, Y.; Vohra, Y. K. Drastic Enhancement of Magnetic Critical Temperature and Amorphization in Topological Magnet EuSn₂P₂ under Pressure. *NPJ Quantum Mater.* **2022**, *7* (1), 43.

(53) Manghnani, H. M.; Syono, Y. *High-Pressure Research in Mineral Physics: A Volume in Honor of Syun-Iti Akimoto*; Manghnani, M. H., Syono, Y., Eds.; Terra Scientific Publishing Company, 1987; pp 347−359.

(54) Mishima, O.; Calvert, L. D.; Whalley, E. 'Melting ice' I at 77 K and 10 kbar: a new method of making amorphous solids. *Nature* **1984**, *310* (5976), 393−395.

(55) Hazen, R. M.; Finger, L. W.; Hemley, R. J.; Mao, H. K. High-Pressure Crystal Chemistry and Amorphization of α-quartz. *Solid State Commun.* **1989**, *72* (5), 507−511.

(56) Wang, S.; Zhu, J.; Zhang, Y.; Yu, X.; Zhang, J.; Wang, W.; Bai, L.; Qian, J.; Yin, L.; Sullivan, N. S.; Jin, C.; He, D.; Xu, J.; Zhao, Y. Unusual Mott Transition in Multiferroic PbCrO₃. *Proc. Natl. Acad. Sci. U.S.A.* **2015**, *112* (50), 15320−15325.

(57) Leonov, I.; Belozerov, A. S.; Skornyakov, S. L. Unusual Mott Transition Associated with Charge-Order Melting in BiNiO₃ under Pressure. *Phys. Rev. B* **2019**, *100* (16), 161112.

(58) Oka, K.; Mizumaki, M.; Sakaguchi, C.; Sinclair, A.; Ritter, C.; Attfield, J. P.; Azuma, M. Intermetallic Charge-Transfer Transition in Bi₁₋ₓLaₓNiO₃ as the Origin of the Colossal Negative Thermal Expansion. *Phys. Rev. B: Condens. Matter Mater. Phys.* **2013**, *88* (1), 014112.

(59) Woodward, P. M.; Cox, D. E.; Moshopoulou, E.; Sleight, A. W.; Morimoto, S. Structural Studies of Charge Disproportionation and Magnetic Order in CaFeO₃. *Phys. Rev. B: Condens. Matter Mater. Phys.* **2000**, *62* (2), 844−855.

(60) Hayashi, N.; Yamamoto, T.; Kageyama, H.; Nishi, M.; Watanabe, Y.; Kawakami, T.; Matsushita, Y.; Fujimori, A.; Takano, M. BaFeO₃: A Ferromagnetic Iron Oxide. *Angew. Chem., Int. Ed.* **2011**, *50* (52), 12547−12550.

(61) Yang, J. B.; Kim, M. S.; Cai, Q.; Zhou, X. D.; Anderson, H. U.; James, W. J.; Yelon, W. B. Study of the Electronic Structure of CaFeO₃. *J. Appl. Phys.* **2005**, *97* (10), 10A312.

(62) Hoedl, M. F.; Ertural, C.; Merkle, R.; Dronskowski, R.; Maier, J. The Orbital Nature of Electron Holes in BaFeO₃ and Implications for Defect Chemistry. *J. Phys. Chem. C* **2022**, *126* (30), 12809−12819.

(63) Paul, A.; Mukherjee, A.; Dasgupta, I.; Paramekanti, A.; Saha-Dasgupta, T. Hybridization-Switching Induced Mott Transition in ABO₃ Perovskites. *Phys. Rev. Lett.* **2019**, *122* (1), 016404.